

Dinuclear Iron(III) and Cobalt(III) Complexes Featuring a Biradical Bridge: Their Molecular Structures and Magnetic, Spectroscopic, and Redox Properties

Dhrubajyoti Mondal,[†] Mithun Chandra Majee,[†] Sanchita Kundu,[†] Max Mörtel,[§] Ghulam Abbas,[§] Akira Endo,[‡] Marat M. Khusniyarov,^{*,§,§} and Muktimoy Chaudhury^{*,†,†}

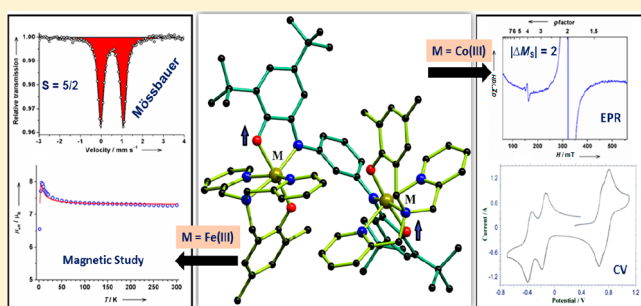
[†]Department of Inorganic Chemistry, Indian Association for the Cultivation of Science, Jadavpur, Kolkata 700 032, India

[‡]Department of Materials and Life Sciences, Faculty of Science and Technology, Sophia University, 7-1 Kioi-cho, Chiyoda-ku, Tokyo 102-8554, Japan

[§]Department of Chemistry and Pharmacy, Friedrich-Alexander University Erlangen-Nürnberg (FAU), Egerlandstrasse 1, 91058 Erlangen, Germany

Supporting Information

ABSTRACT: Bis-bidentate ligand H_4L^B featuring two *o*-amidophenol noninnocent units was used to synthesize novel binuclear complexes $[(L^R)M^{III}(\bullet L^B \bullet)M^{III}(L^R)](ClO_4)_2$, $M = Fe$ (**1**) and Co (**2**, **3**), with HL^R ($R = CH_3, Cl$) being the facially coordinating tetradentate coligands. Upon the synthesis, the fully reduced amidophenolate form of the ligand $(L^B)^{4-}$ becomes oxidized, resulting in the formation of a rare example of a biradical $(\bullet L^B \bullet)^{2-}$ bridge connecting two metal ions, as supported by X-ray crystallography. The electronic structures of the complexes have been probed by Mössbauer spectroscopy, magnetic susceptibility measurements, and electron paramagnetic resonance (EPR) spectroscopy. Species **1** contains two high-spin Fe(III) ions ($S = 5/2$) each coupled strongly antiferromagnetically ($|J| > 150 \text{ cm}^{-1}$; $\hat{H} = -2\hat{S}_1\hat{S}_2$) with a semiquinone π -radical ($S = 1/2$) form of the bridging $(\bullet L^B \bullet)^{2-}$ ligand. The effective $S = 2$ spins of each $[Fe(III)+R^\bullet]$ monomeric unit are then weakly ferromagnetically coupled with $J = +0.22 \text{ cm}^{-1}$. Species **2** and **3** reveal very similar electronic structures: the low-spin Co(III) ion is diamagnetic, which leaves the two-spin carriers at the bridging $(\bullet L^B \bullet)^{2-}$ biradical to display an isotropic EPR signal at $g = 1.995$ for **2** (1.993 for **3**) in solution at room temperature and in the frozen state with no hyperfine structure. The weak half-field signal at $g = 3.988$ for **2** (3.978 for **3**) was also observed at 17 K for the spin-forbidden $|\Delta M_S| = 2$ transition due to ferromagnetically coupled $S = 1/2$ spins ($J = +47 \text{ cm}^{-1}$) of the bridging biradical. The compounds show rich electrochemistry, displaying two (**1**) or four (**2**, **3**) one-electron reversible processes. Normal and differential pulse voltammetry as well as constant potential coulometry, combined with EPR experiments, confirmed that the observed electron transfers are all localized at the bridging noninnocent $(\bullet L^B \bullet)^{2-}$ ligand.



1 contains two high-spin Fe(III) ions ($S = 5/2$) each coupled strongly antiferromagnetically ($|J| > 150 \text{ cm}^{-1}$; $\hat{H} = -2\hat{S}_1\hat{S}_2$) with a semiquinone π -radical ($S = 1/2$) form of the bridging $(\bullet L^B \bullet)^{2-}$ ligand. The effective $S = 2$ spins of each $[Fe(III)+R^\bullet]$ monomeric unit are then weakly ferromagnetically coupled with $J = +0.22 \text{ cm}^{-1}$. Species **2** and **3** reveal very similar electronic structures: the low-spin Co(III) ion is diamagnetic, which leaves the two-spin carriers at the bridging $(\bullet L^B \bullet)^{2-}$ biradical to display an isotropic EPR signal at $g = 1.995$ for **2** (1.993 for **3**) in solution at room temperature and in the frozen state with no hyperfine structure. The weak half-field signal at $g = 3.988$ for **2** (3.978 for **3**) was also observed at 17 K for the spin-forbidden $|\Delta M_S| = 2$ transition due to ferromagnetically coupled $S = 1/2$ spins ($J = +47 \text{ cm}^{-1}$) of the bridging biradical. The compounds show rich electrochemistry, displaying two (**1**) or four (**2**, **3**) one-electron reversible processes. Normal and differential pulse voltammetry as well as constant potential coulometry, combined with EPR experiments, confirmed that the observed electron transfers are all localized at the bridging noninnocent $(\bullet L^B \bullet)^{2-}$ ligand.

INTRODUCTION

Interactions between metal complexes with radical ligands have been a topic of contemporary research interest.¹ Many metalloenzymes couple one-electron redox changes at metal centers with redox-active ligands to promote multielectron chemistry.² Such redox-active ligands were classified by Jørgensen as “noninnocent” ligands.³ Some of these systems including the $O_2/O_2^{\bullet-}/O_2^{2-}$, $NO^+/NO^\bullet/NO^-$, *o*-quinone/*o*-semiquinone/catecholate, tyrosyl/tyrosinate, tetrapyrrole macrocycles (porphyrins, chlorins, and corroles), pterins, flavins, and the dithiolene/ene-dithiolate ligands are ubiquitous in biology, which require transition metal ions to play critical roles in sustaining our life processes.⁴ To understand more about the intricate bioinorganic chemistry underlying those biological processes, it is imperative to know more about the basic coordination chemistry of transition metal ions involving

radical ligands, which turns out to be one of the thrust areas in contemporary coordination chemistry research.

Probably the most researched noninnocent ligands are catecholate/*o*-quinone redox systems,^{1a,5} with the radical *o*-semiquinone as the frequently isolated intermediate form. Their isoelectronic aza analogues in their dianionic forms, viz. 2-amidophenoxide and 1,2-diamidobenzene, are also prone to one- or two-electron oxidation to form monoanionic (imino)-semiquinones or neutral (imino)benzoquinones, which also appear to be highly interesting considering their relevance to biochemistry.^{6–9} Furthermore, the ligand radicals stabilized by coordinated metal ions are interesting from the magnetic point of view and provide many exciting examples of spin-coupled systems.¹⁰ A good number of interesting works have been

Received: September 11, 2017

reported recently with redox-active bridging ligands capable of forming radical-bridged bimetallic complexes.^{11–18} Interestingly, however, very few discrete, soluble biradical-bridged metal complexes have been reported thus far.^{15,19}

Our objective in this work is to synthesize binuclear complexes with biradicals as a bridge between the coordinating metal ions, considering their paucity in the existing literature. Such complexes of early transition metal ions with noninnocent ligands are expected to display sophisticated magnetic and spectroscopic properties. A bis-bidentate ligand, viz. *N,N'*-bis(3,5-di-*tert*-butyl-2-hydroxyphenyl)-1,3-phenylenediamine (H_4L^B), containing a pair of redox noninnocent aminophenol arms linked to a metaphenylene moiety has been identified to bridge the participating metal centers. Once completely deprotonated, this ligand can undergo a series of oxidative transformations to generate a four-electron redox chain that includes a SQ–SQ (SQ = iminobenzosemiquinone) biradical as one of the several options.²⁰ We harnessed this possibility to synthesize the biradical-bridged complexes $[(L^R)M](\bullet L^B \bullet)\{M(L^R)\}(ClO_4)_2$ of Fe^{III} (**1**) and Co^{III} (**2** and **3**) using a facially coordinating phenol-based tetradentate ligand HL^R ($R = Me$ or Cl) in tandem with the bridging H_4L^B coligand, with the latter undergoing a two-electron oxidation to form a rare example of a biradical $(\bullet L^B \bullet)^{2-}$ bridge. The magnetic, electron paramagnetic resonance (EPR), and electrochemical properties of these complexes have been studied in detail to understand their electronic structures.

EXPERIMENTAL SECTION

Materials. The solvents were reagent grade, dried by standard procedure,²¹ and distilled under nitrogen prior to their use. Reagent-grade chemicals were purchased from commercial sources and used as received.

Synthesis of Ligands. The proligands HL^{Me} and HL^{Cl} were prepared by Mannich reaction following a modified procedure of a reported method.²² The bridging ligand *N,N'*-bis(3,5-di-*tert*-butyl-2-hydroxyphenyl)-1,3-phenylenediamine (H_4L^B) was also synthesized following a reported procedure.²⁰

***N*-(3,5-Dimethyl-2-hydroxybenzyl)-*N,N'*-bis(2-pyridylmethyl)amine (HL^{Me}).** Dipicolylamine (2.00 g, 10 mmol), paraformaldehyde (0.3 g, 10 mmol), and 2,4-dimethylphenol (1.22 g, 10 mmol) were taken in methanol (50 mL). The solution was heated under reflux for ca. 20 h and then cooled to 4 °C. The evaporation of the solvent under reduced pressure gave a yellow oil, which was solidified by scratching with a glass rod. The resulting solid was crystallized from a dichloromethane/methanol (2:1 v/v) mixture to obtain a white crystalline compound. Yield: 2.7 g (82%); mp, 165 °C. Anal. Calcd for $C_{21}H_{23}N_3O$: C, 75.65; H, 6.95; N, 12.60. Found: C, 75.80; H, 7.10; N, 12.57%. ¹H NMR (400 MHz, $CDCl_3$, δ /ppm): 2.20 (s, 3H, CH_3 of Me), 2.25 (s, 3H, CH_3 of Me), 3.75 (s, 2H, Ph- CH_2), 3.85 (s, 4H, Py- CH_2), 6.70 (s, 1H, aryl), 6.86 (s, 1H, aryl), 7.13 (m, 2H, py), 7.34 (d, 2H, py), 7.60 (m, 2H, py), 8.56 (d, 2H, py), 10.63 (broad, 1H, Ph-OH). ESI-MS (positive) in CH_3CN : m/z 334.30 (100%, $M + H^+$).

***N*-(3,5-Dichloro-2-hydroxybenzyl)-*N,N'*-bis(2-pyridylmethyl)amine (HL^{Cl}).** This ligand was synthesized following the same procedure as that described above for HL^{Me} using 2,4-chlorophenol as a replacement for 2,4-dimethylphenol. Yield: 72%; mp, 152 °C. Anal. Calcd for $C_{19}H_{17}Cl_2N_3O$: C, 60.97; H, 4.58; N, 11.23. Found: C, 60.80; H, 4.50; N, 11.20%. ¹H NMR (400 MHz, $CDCl_3$, δ /ppm): 3.77 (s, 2H, Ph- CH_2), 3.88 (s, 4H, Py- CH_2), 6.97 (d, 1H, aryl), 7.17 (m, 2H, py), 7.27 (d, 1H, aryl), 7.30 (d, 2H, py), 7.64 (m, 2H, py), 8.59 (d, 2H, py), 12.32 (broad, 1H, Ph-OH). ESI-MS (positive) in CH_3CN : m/z 374.40 (100%, $M + H^+$).

Preparation of Complexes. *Safety Note! Caution!* Perchlorate salts of metal complexes are potentially explosive and should be handled in small quantities with sufficient care.²³

$[(L^{Me})Fe^{III}(\bullet L^B \bullet)Fe^{III}(L^{Me})][ClO_4]_2 \cdot 4CH_3OH$ (**1**). The proligand HL^{Me} (83 mg, 0.25 mmol) was dissolved in 25 mL of methanol followed by the additions of $Fe(ClO_4)_2 \cdot 6H_2O$ (92 mg, 0.25 mmol) and triethylamine (25 mg, 0.25 mmol). The pink colored reaction mixture was stirred for 30 min. To this stirred solution was added dropwise a methanolic solution (5 mL) of the bridging ligand H_4L^B (65 mg, 0.13 mmol), deprotonated completely with 4 equiv of triethylamine (50 mg, 0.5 mmol). The resulting mixture was refluxed for 2 h when a dark brown solution was obtained. It was filtered, and the filtrate was kept in the open air for slow evaporation. After 7 days, block-shaped dark brown crystalline product was collected by filtration. Some of these crystals were of diffraction grade and used directly for X-ray crystallographic analysis. The compound is prone to solvent loss. Drying under vacuum for a long time afforded a fully desolvated analytical-grade sample that was used subsequently for microanalysis and some other measurements. Yield: 120 mg (65%). Anal. Calcd for $C_{76}H_{88}N_8O_{12}Cl_2Fe_2$: C, 61.34; H, 5.96; N, 7.53. Found: C, 61.19; H, 5.85; N, 7.55%. FT-IR bands (KBr pellets, cm^{-1}): 2954(m), 1606(m), 1469(m), 1444(m), 1251(m), 1093(s), 802(m), 622(m). UV–vis [CH_2Cl_2 ; λ_{max} nm (ϵ , $L mol^{-1} cm^{-1}$): 855 (11550), 527 (5500), 438 (7400), 346 (18700).

$[(L^{Me})Co^{III}(\bullet L^B \bullet)Co^{III}(L^{Me})][ClO_4]_2 \cdot 2CH_3OH \cdot 2H_2O$ (**2**). This compound was prepared in a manner similar to that for **1** using $Co(ClO_4)_2 \cdot 6H_2O$ instead of $Fe(ClO_4)_2 \cdot 6H_2O$ as the metal ion precursor. A brown block-shaped crystalline compound was obtained within 7 days. Some of the available crystals were of diffraction quality and used directly for X-ray crystal structure analysis. Yield: 55%. Here, we also used a desolvated sample for microanalysis as we did for compound **1**. Anal. Calcd for $C_{76}H_{88}N_8O_{12}Cl_2Co_2$: C, 61.09; H, 5.94; N, 7.50. Found: C, 60.76; H, 5.75; N, 7.28%. FT-IR bands (KBr pellets, cm^{-1}): 2956(m), 1610(m), 1471(m), 1421(m), 1257(m), 1091(s), 769(m), 622(m). UV–vis [CH_2Cl_2 ; λ_{max} nm (ϵ , $L mol^{-1} cm^{-1}$): 956 (2250), 842 (2700), 734 (2750), 644 (3750), 515 (10200), 489 (11000).

$[(L^{Cl})Co^{III}(\bullet L^B \bullet)Co^{III}(L^{Cl})][ClO_4]_2 \cdot 2CH_2Cl_2$ (**3**). This compound was prepared following a procedure similar to that described above for compound **2** using the proligand HL^{Cl} instead of HL^{Me} . Diffraction quality crystals were grown from a dichloromethane/methanol mixture (1:1 v/v). We used a desolvated sample for microanalysis as we did for compound **1**. Yield: 56%. Anal. Calcd for $C_{72}H_{76}N_8O_{12}Cl_6Co_2$: C, 54.87; H, 4.86; N, 7.11. Found: C, 53.92; H, 4.72; N, 6.67%. FT-IR bands (KBr pellets, cm^{-1}): 2960(m), 1612(m), 1452(s), 1429(m), 1315(m), 1091(s), 765(m), 626(m). UV–vis [CH_2Cl_2 ; λ_{max} nm (ϵ , $L mol^{-1} cm^{-1}$): 947 (3100), 842 (3350), 740 (2100), 609 (3100), 514 (8950), 483 (11000).

Physical Measurements. IR spectroscopic measurements were made on samples pressed into KBr pellets using a Shimadzu 8400S FT-IR spectrometer, whereas for UV–visible spectral measurements, a PerkinElmer Lambda 950 UV/vis/NIR spectrophotometer was employed. Elemental analyses (for C, H, and N) were performed at IACS on a PerkinElmer model 2400 series II CHNS analyzer. The electrospray ionization mass spectra (ESI-MS) in positive ion mode were measured on a Micromass QTOF model YA 263 mass spectrometer. The ¹H NMR spectra were recorded on a Bruker model Avance DPX-400 spectrometer using TMS as the internal standard. X-band EPR measurements were performed on a JEOL JES-FA 200 instrument. Cyclic voltammetry (CV) in acetonitrile solution was recorded on a BAS model 100B/W electrochemical workstation using a glassy carbon disk (i.d. = 1.6 mm) as working electrode and a platinum wire counter electrode. Ag/AgCl (3 M aqueous NaCl) electrode was used for reference and Fc/Fc^+ couple as the internal standard.²⁴ Solutions were ~1.0 mM in samples and contained 0.1 M TBAP as supporting electrolyte. Under the present experimental condition, the Fc/Fc^+ couple was located at 0.45 V. Bulk electrolysis was carried out using a platinum gauze working electrode.

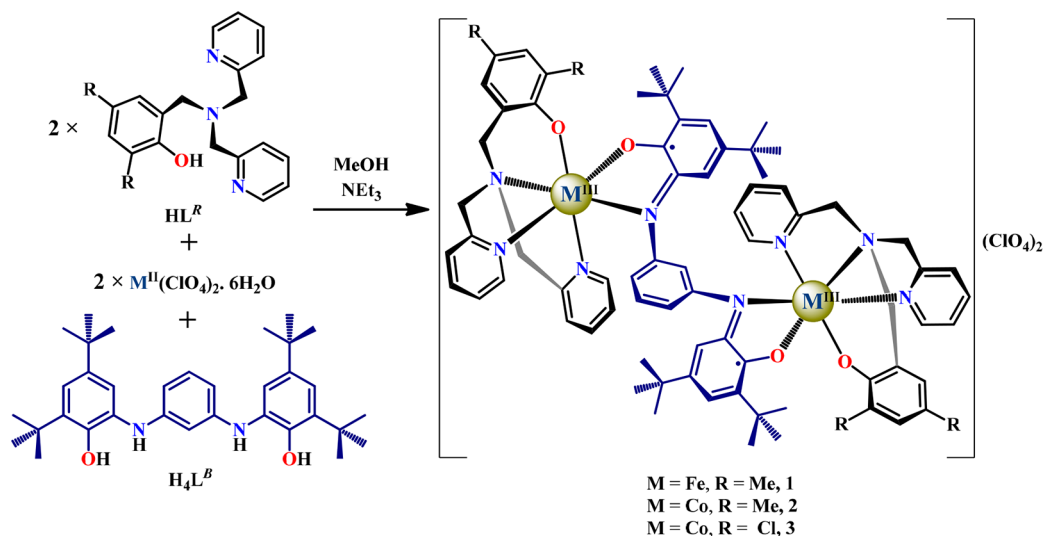
⁵⁷Fe Mössbauer spectra were recorded at 77 K in constant acceleration mode on a WissE1 Mössbauer spectrometer (MRG-500). ⁵⁷Co/Rh was used as the radiation source. MFIT software was used for the quantitative evaluation of the spectral parameters.²⁵ The temperature of the samples was controlled by an MBBC-HE0106

Table 1. Summary of Crystallographic Data for Complexes of 1, 2, and 3

parameters	1	2	3
composition	C ₇₆ H ₈₈ N ₈ O ₁₂ Cl ₂ Fe ₂ ·4CH ₃ OH	C ₇₆ H ₈₈ N ₈ O ₁₂ Cl ₂ Co ₂ ·2CH ₃ OH·2H ₂ O	C ₇₂ H ₇₆ N ₈ O ₁₂ Cl ₆ Co ₂ ·2CH ₂ Cl ₂
formula wt	1616.31	1590.38	1745.82
crystal system	monoclinic	monoclinic	monoclinic
space group	C2/c	C2/c	C2/c
a, Å	24.2428(15)	24.401(16)	24.922(2)
b, Å	11.7328(7)	11.476(8)	11.4488(11)
c, Å	27.7714(17)	27.186(17)	27.418(3)
α, deg	90	90	90
β, deg	99.9354(14)	99.311(9)	100.053(2)
γ, deg	90	90	90
V, Å ³	7780.7(8)	7512(9)	7703.0(13)
ρ _{calc} , Mg m ⁻³	1.380	1.406	1.505
temp, K	150(2)	150(2)	150(2)
λ (Mo Kα), Å	0.71073	0.71073	0.71073
Z	4	4	4
F(000)/μ mm ⁻¹	3416/0.504	3344/0.586	3600/0.844
2θ _{max} [deg]	56.084	48.682	53.294
reflections collected/unique	41494/9081	23962/5901	39555/7967
R _{int} /GOF on F ²	0.0803/1.369	0.1181/1.900	0.0905/2.618
no. of parameters	500	474	485
R1 ^a (F _o), wR2 ^b (F _o) (all data)	0.0580, 0.1823	0.0869/0.1557	0.0649, 0.1174
largest diff. peak, deepest hole, e Å ⁻³	0.787, -0.997	1.142, -0.774	1.143, -1.038

$${}^a R = \sum ||F_o| - |F_c|| / \sum |F_o|. \quad {}^b wR = [\sum [w((F_o^2 - F_c^2)^2)] / \sum w(F_o^2)^2]^{1/2}.$$

Scheme 1. Schematic Presentation of the Synthesis of Biradical-Bridged Complexes



Mössbauer He/N₂ cryostat within an accuracy of ±0.3 K. Isomer shifts were determined relative to α-iron at 298 K. Magnetic susceptibility data on solid samples were collected using a Quantum Design MPMS-XL SQUID magnetometer. The data were obtained for microcrystalline samples restrained within a polycarbonate gel capsule. DC susceptibility data were collected in the temperature range of 2–300 K and corrected for diamagnetism. The program *JuIX* was used for the simulation and analysis of magnetic data.²⁶

Theoretical Calculations. Program ORCA 4.0.0 was used for all spin-unrestricted density functional theory (DFT) calculations.²⁷ The calculations on complexes 1–3 were performed on simplified models with all *tert*-Bu groups truncated to Me groups. Geometry optimization and single-point calculations were done with the B3LYP functional^{28,29} using def2-TZVP and def2-SVP basis sets³⁰ for non-C/H and C/H atoms, respectively. RIJCOSX approximations with appropriate auxiliary basis sets (def2/J)³¹ were employed for all calculations. Broken symmetry (BS) formalism was used; the iron

complex 1 was calculated as the BS(10,2) state, whereas the cobalt complexes 2 and 3 were calculated as BS(1,1) states. Time-dependent (TD)-DFT calculations were accomplished with B3LYP using slightly reduced basis sets: def2-TZVP and def2-SVP for metal and nonmetal atoms, respectively. The first 40 excited states were calculated for each complex. Molecular orbitals and spin density maps were visualized with Molekel.³²

X-ray Crystallography. Suitable crystals of 1 (dark brown block, 0.18 × 0.15 × 0.14 mm³), 2 (dark brown block, 0.15 × 0.12 × 0.12 mm³), and 3 (dark brown block, 0.18 × 0.16 × 0.10 mm³) were mounted on glass fibers and coated with perfluoropolyether oil before mounting. Intensity data for the aligned crystals were measured employing a Bruker SMART APEX II CCD diffractometer equipped with a monochromatized Mo Kα radiation (λ = 0.71073 Å) source at 150(2) K. No crystal decay was observed during the data collections. In all cases, absorption corrections based on multiscans using the SADABS software³³ were applied. The structures were solved by direct

methods³⁴ and refined on F^2 by a full-matrix least-squares procedure based on all data minimizing $wR = [\sum[w(F_o^2 - F_c^2)^2]/\sum(F_o^2)^2]^{1/2}$, $R = \sum ||F_o| - |F_c||/\sum|F_o|$, and $S = [\sum[w(F_o^2 - F_c^2)^2]/(n - p)]^{1/2}$. SHELXL-2013 was used for both structure solutions and refinements.³⁵ All non-hydrogen atoms were refined anisotropically. The hydrogen atoms were calculated and isotropically fixed in the final refinement [$d(C-H) = 0.95 \text{ \AA}$, with the isotropic thermal parameter of $U_{iso}(H) = 1.2U_{iso}(C)$]. The SMART and SAINT software packages³⁶ were used for data collection and reduction, respectively. Crystallographic diagrams were drawn using the DIAMOND software package.³⁷ A summary of the relevant crystallographic data and the final refinement details are given in Table 1.

RESULTS AND DISCUSSION

Synthesis. The binuclear complexes $[(L^R)M^{III}(\bullet L^B \bullet)]M^{III}(L^R)[ClO_4]_2$; $M = Fe$ (1) and Co (2, 3) containing a biradical bridge $(\bullet L^B \bullet)^{2-}$ have been synthesized as crystalline solids in moderate yields (55–65%) in a single-step reaction by mixing together $M^{II}(ClO_4)_2 \cdot 6H_2O$, tetradentate capping ligand HL^R , and the redox-active bis-bidentate bridging ligand H_4L^B in a 2:2:1 molar ratio under aerobic conditions in methanol (Scheme 1). During the reaction, the metal ions are oxidized from their initial +2 to +3 state, and the bridging ligand is oxidized from its initial $(L^B)^{4-}$ to the biradical $(\bullet L^B \bullet)^{2-}$ state, with aerial oxygen being the oxidant in both cases. Perchlorate ions act as the counteranion to balance the charge of these cationic complexes. Compounds 1–3 are stable indefinitely in the solid state when stored in a desiccator and are soluble in most common organic solvents, including methylene chloride, acetone, and acetonitrile.

The complexes show prominent IR absorption peaks around 2960 cm^{-1} due to the stretching C–H bonds of *tert*-butyl group. Perchlorate anion exhibits its fingerprints due to stretching and bending modes at 1090 and 690 cm^{-1} , respectively. The band around 1600 cm^{-1} is due to pyridine moiety of the capping tetradentate ligand.

Description of Crystal Structures. The X-ray crystal structure of the cationic form of the iron complex 1 is shown in Figure 1. The oxidation states of the metal centers and the bridging noninnocent ligand can be assigned comfortably from the metrical parameters, summarized in Table 2. Complex 1 crystallizes in the monoclinic space group $C2/c$ with four molecular mass units accommodated per cell. The molecule has a two-fold symmetry, and the asymmetric unit contains one-half of the entire molecule generated by the symmetry axis passing

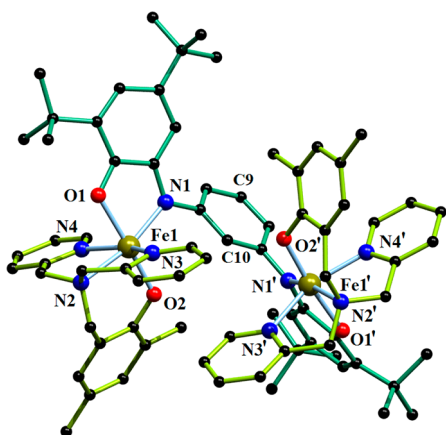


Figure 1. Perspective view of the molecular structure of the cationic complex in 1. H atoms have been omitted for clarity.

Table 2. Selected Bond Distances and Angles in Complexes 1, 2, and 3

	bond lengths (Å)		
	1	2	3
M1–O1	2.048(2)	1.912(4)	1.894(2)
M1–O2	1.890(2)	1.898(4)	1.906(2)
M1–N1	2.021(2)	1.936(5)	1.950(3)
M1–N2	2.195(2)	1.949(5)	1.967(3)
M1–N3	2.156(2)	1.913(5)	1.959(3)
M1–N4	2.135(2)	1.949(5)	1.933(3)
	bond angles (deg)		
	1	2	3
O2–M1–N1	101.31(8)	93.04(17)	93.29(10)
O2–M1–O1	174.34(8)	176.66(17)	176.67(10)
N1–M1–O1	78.74(8)	84.24(17)	84.54(10)
O2–M1–N4	91.47(9)	92.61(17)	90.82(11)
N1–M1–N4	101.62(8)	95.41(19)	95.92(12)
O1–M1–N4	83.00(8)	89.58(18)	86.90(11)
O2–M1–N3	96.85(8)	91.41(18)	92.89(11)
N1–M1–N3	101.29(9)	95.6(2)	94.96(11)
O1–M1–N3	88.67(8)	86.94(18)	89.82(11)
N4–M1–N3	153.54(9)	168.1(2)	168.29(12)
O2–M1–N2	92.83(8)	94.19(19)	94.12(11)
N1–M1–N2	165.86(9)	172.7(2)	172.52(12)
O1–M1–N2	87.17(8)	88.55(19)	88.10(11)
N4–M1–N2	77.52(8)	83.5(2)	84.93(13)
N3–M1–N2	77.02(9)	85.0(2)	83.72(12)

along the C9 and C10 atoms of the bridging *meta*-phenylene ring (Figure 1). The coordination geometry around the individual iron centers is a distorted octahedron in which the basal plane is occupied by N1, N2, N3, and N4 donor atoms, and the axial sites are occupied by O1 and O2 atoms. The N2, N3, N4, and O2 donor atoms come from the facially coordinated tetradentate capping ligand, and the N1 and O1 sites originate from the bis-bidentate bridging ligand. The relatively long metal–ligand bond distances ($Fe-O_{phenolate} = 1.890(2) \text{ \AA}$, $Fe-N_{amine} = 2.021(2) \text{ \AA}$, and the av. $Fe-N_{pyridine} = 2.1455 \text{ \AA}$) are all consistent with a high-spin d^5 iron(III) center,³⁸ as supported further by Mössbauer data (vide infra).

The metrical data also provide interesting clues to the oxidation state of the bridging redox noninnocent ligand, which, in principle, can exist in one or more of the amidophenolate (L^{AP}^{2-}), iminobenzosemiquinone (L^{ISQ}^{1-}), and iminobenzoquinone (L^{IBQ}^0) forms,³⁹ as displayed in Figure 2. The C–C bond distances between the ring carbon atoms of the *tert*-butyl-containing C_6 rings in complex 1 are found to be unequal, involving two alternating short C–C bonds (C2–C3 and C4–C5) along with four longer C–C distances (C1–C2, C3–C4, C5–C6, and C6–C1) as summarized in Table 3. Additionally, the C(1)–O(1) $1.283(3) \text{ \AA}$ and C(6)–N(1) $1.342(3) \text{ \AA}$ bond distances are lying in the ranges, somewhat intermediate between their single and double bond characters, thus supporting the one-electron oxidized iminobenzo-semiquinone state of both bidentate coordination sites of this bis-bidentate bridging moiety.³⁹ Therefore, from the single-crystal X-ray analysis, complex 1 can be described as a high-spin diferric complex $[(L^{Me})Fe^{III}(\bullet L^B \bullet)Fe^{III}(L^{Me})](ClO_4)_2$ containing a biradical bridge.

The Co(III) complexes 2 and 3 are isostructural, and both crystallize in the same space group $C2/c$ with four molecular

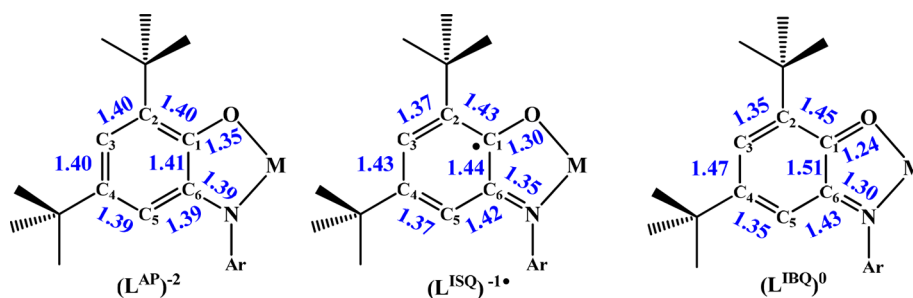


Figure 2. Average bond distances (Å) in N,O-coordinated ligands ($(L^{AP})^{2-}$), ($(L^{ISQ})^{-1\bullet}$), and ($(L^{IBQ})^0$) as determined by X-ray crystallography.³⁹

Table 3. Bond Lengths (Å) in the Iminobenzosemiquinonate Moieties of Complexes 1, 2, and 3

	O1–C1	N1–C6	C1–C2	C2–C3	C3–C4	C4–C5	C5–C6	C6–C1
1	1.283(3)	1.342(3)	1.434(4)	1.367(4)	1.431(4)	1.362(4)	1.421(4)	1.463(4)
2	1.307(6)	1.342(7)	1.414(8)	1.362(8)	1.426(8)	1.368(8)	1.420(8)	1.434(7)
3	1.311(4)	1.365(4)	1.408(5)	1.370(5)	1.425(5)	1.362(4)	1.414(4)	1.440(4)

mass units per unit cell (Table 1). The perspective view of the molecular structure of a representative Co(III) compound 2 is shown in Figure 3 and that of 3 in Figure S1 (Supporting

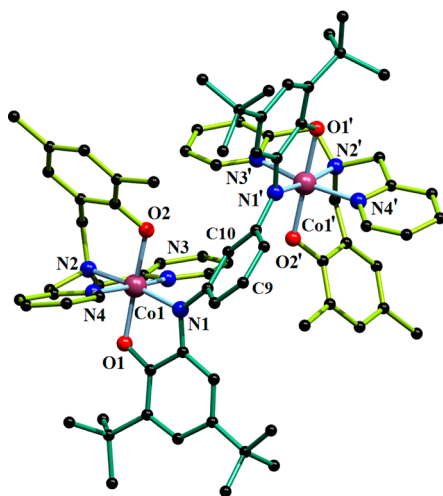


Figure 3. Perspective view of the molecular structure of the cationic complex in 2. H atoms have been omitted for clarity.

Information). Identical atom labeling schemes have been adopted for both the structures for the easy comparison of their metrical parameters (Table 2). Both compounds have a two-fold axis of symmetry that bisects the bridging phenylene ring into two identical halves, each involving a cobalt(III) ion with a distorted octahedral geometry similar to 1. The basal plane surrounding the Co1 center is made up of the pyridine nitrogen atoms N3 and N4 and the amino nitrogen N2, all coming from the facially coordinating tetradentate ligand (L^{Me})⁻, along with the donor N1 contributed by the bridging bis-bidentate ligand. The apical sites are taken up by the phenolate oxygen donors O1 and O2, contributed by the bridging and the capping ligand, respectively. The measured distances Co–O_{phenolate}, Co–N_{amine}, and Co–N_{pyridine} are 1.898(4), 1.949(5), and 1.931(5) Å, respectively. Corresponding distances in 3 are 1.906(2), 1.967(3), and 1.946(3) Å, respectively, which again are consistent with a low-spin d⁶ cobalt(III) center in these two complexes.⁴⁰

The C–O, C–N, and internal ring C–C bond distances (Table 3) also support the iminobenzosemiquinonate ($(L^{ISQ})^{-1\bullet}$) state for each of the bidentate arms of the bridging ligand as observed in 1. Thus, the electronic structures of the cobalt complexes 2 and 3 are [$(L^{Me})Co^{III}(\bullet L^B\bullet)Co^{III}(L^{Me})$](ClO₄)₂ and [$(L^{Cl})Co^{III}(\bullet L^B\bullet)Co^{III}(L^{Cl})$](ClO₄)₂, respectively, involving two low-spin Co(III) centers connected by a biradical bridge.

The structure of 1 features an intramolecular Fe...Fe separation of 6.038 Å and a closest intermolecular Fe...Fe separation of 10.717 Å. Similarly, the intramolecular and closest intermolecular Co...Co distance are 6.304 and 10.469 Å, respectively, for complex 2 and 6.376 and 10.704 Å, respectively, for complex 3.

Another important feature observed in 1–3 is the abundance of intermolecular contacts between the two neighboring molecules in the crystal lattice. Close π ... π and C–H... π interactions of the pyridine rings of 1 organize these dinuclear units into a ribbon-like assembly along the crystallographic *c*-axis (Figure 4). Perchlorate anions, needed to counterbalance the charge of these dinuclear cationic complexes, also play a significant role in generating the three-dimensional structure of these molecules. These anions are positioned between the two

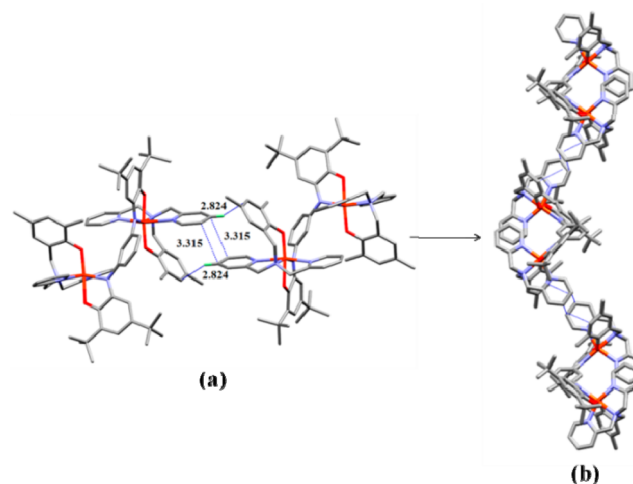


Figure 4. Solid-state structure of 1 showing (a) intermolecular stacking interactions and (b) ribbon-like assembly.

parallel ribbons and through weak C–H⋯anion interactions, generating the whole three-dimensional structure of this molecule (Figure 5). Complexes 2 and 3 also exhibit identical types of stacking interactions, leading to the formation of similar double-ribbon-like assembly (Figure S2).

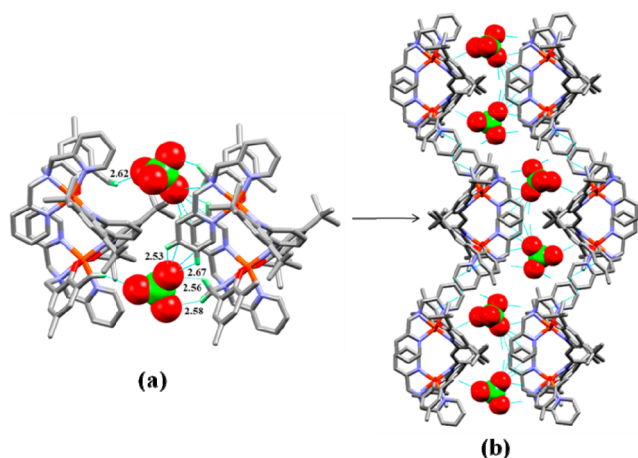


Figure 5. Solid-state structure of **1** showing (a) intermolecular C–H⋯anion interactions leading to an extended structure and (b) view of the double-ribbon extended structure.

Electronic Absorption Spectroscopy. Electronic absorption spectra of complexes **1–3** have been recorded in dichloromethane solutions. Spectra in the visible and near-IR region are displayed in Figure 6. All three complexes display

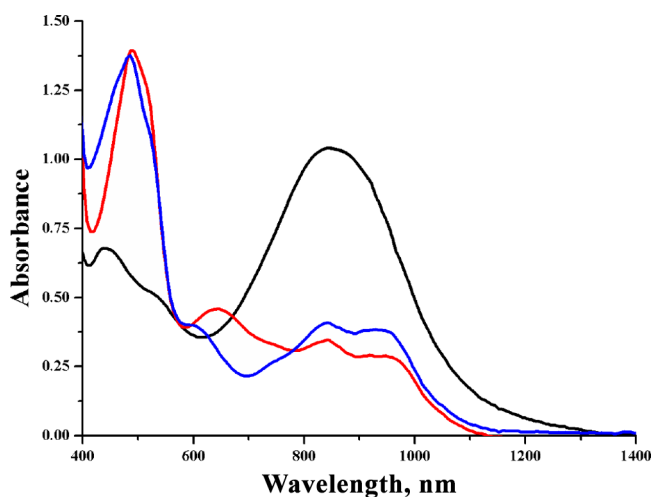


Figure 6. Electronic absorption spectra of complexes **1** (black), **2** (red), and **3** (blue) in dichloromethane solution ($\sim 10^{-4}$ M concentration).

multiple absorption bands, all with high extinction coefficients ($\epsilon = 2200\text{--}19000$ L mol $^{-1}$ cm $^{-1}$) that indicate their charge-transfer origin. Complex **1** exhibits two strong bands at 527 (5500) and 855 nm (11550 L mol $^{-1}$ cm $^{-1}$). The former is likely due to an ligand-to-metal charge transfer (LMCT) transition originating from a PhO \rightarrow Fe(III) charge transfer,⁴¹ whereas the latter band with a broad shape is likely to be originating from a ligand-to-ligand charge transfer (LLCT) as established from DFT calculation (vide infra). Electronic spectra of complexes **2** and **3** are similar, exhibiting several maxima at 956 (2250), 842 (2700), 734 (2750), 644 (3750), 515 (10200),

and 489 nm (11000 L mol $^{-1}$ cm $^{-1}$) for **2**. Corresponding bands for **3** appear at 947 (3100), 842 (3350), 740 (2100), 609 (3100), 514 (8950), and 483 nm (11000 L mol $^{-1}$ cm $^{-1}$), which we believe originate from LMCT, LLCT, and intraligand $\pi\text{--}\pi^*$ transitions within the iminobenzosemiquinone ligands.^{39b,c} All remaining bands appearing in the UV region are most likely due to intraligand transitions.

Mössbauer Spectroscopy. The Mössbauer spectrum of the Fe(III) complex **1** in the solid state at 77 K is shown in Figure 7. The isomer shift (δ) and the quadrupole splitting

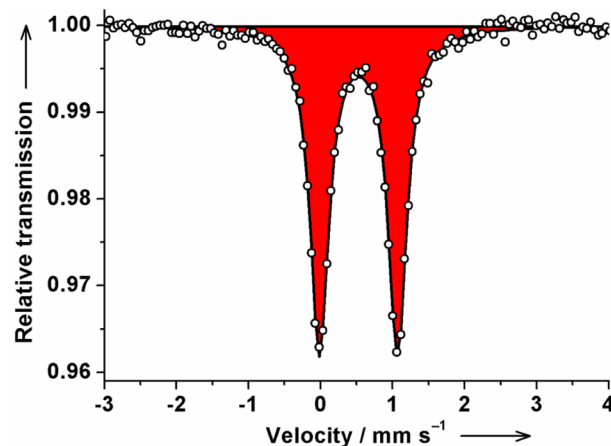


Figure 7. Zero-field ^{57}Fe Mössbauer spectrum of a microcrystalline sample of **1** recorded at 77 K.

parameter ($|\Delta E_Q|$) are 0.53 and 1.08 mm s $^{-1}$, respectively. These values confirm that both the iron ions in **1** are in a high-spin $3d^5$ [$(t_{2g})^3(e_g)^2$] state,⁴² as revealed previously by X-ray crystallography.

EPR Spectroscopy. The X-band EPR spectra of **1–3** were recorded both in liquid solutions (CH_2Cl_2) at room temperature and in frozen solutions ($\text{CH}_2\text{Cl}_2/\text{MeCN}$) at low temperatures. Ferric species **1** was EPR silent in the X-band at all temperatures. This is as expected for a high-spin d^5 metal ion ($S_{\text{Fe}} = 5/2$) coupled strongly antiferromagnetically to a ligand π -radical ($S_{\text{R}} = 1/2$), resulting in an $S = 2$ ground state with an even number of unpaired electrons (vide infra).

Cobalt(III) species **2** and **3** were EPR active in liquid and frozen solutions. The spectra, as expected, are nearly identical. A representative set of spectra for **2** are shown in Figure 8 and those of **3** in Figure S3 (Supporting Information). Room temperature spectra show single isotropic signals at $g = 1.995$ (Figure 8, inset) and 1.993 for **2** and **3**, respectively. The signals remain isotropic at very low temperatures (Figure 8). No hyperfine structure was resolved in both cases. These findings confirm a ligand-based radical character of the cobalt complexes. Importantly, weak half-field signals at $g = 3.978$ and 3.988 were observed at 17 K for **3** and **2**, respectively (Figures 9 and S4). These were assigned to spin-forbidden $|\Delta M_S| = 2$ transitions, which are typical for ferromagnetically coupled organic biradicals ($S = 1/2 + 1/2$).⁴³

Magnetic Studies. Variable-temperature magnetic susceptibility measurements were performed on microcrystalline solid samples of **1–3**. The effective magnetic moment (μ_{eff}) of **1** at room temperature is 7.29 μ_{B} , which remains nearly constant in the temperature range of 70–300 K (Figure 10). At lower temperatures, the moment increases gradually to 7.96 μ_{B} at 7 K, followed by a rapid drop to 6.55 μ_{B} at 2 K. The plateau at 7.29

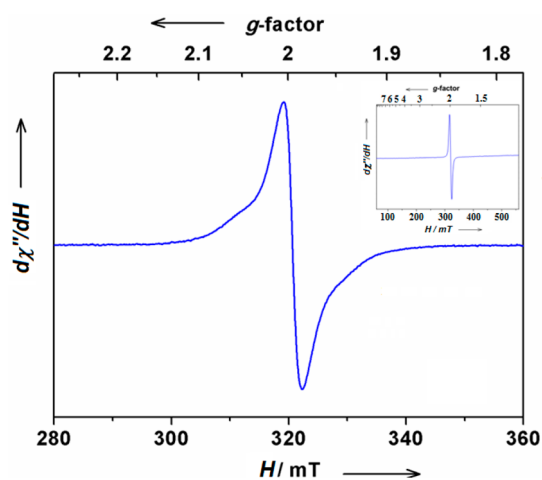


Figure 8. Frozen solution ($\text{CH}_2\text{Cl}_2/\text{MeCN}$) X-band EPR spectrum of **2**, measured at 17 K. Inset: Spectrum at room temperature.

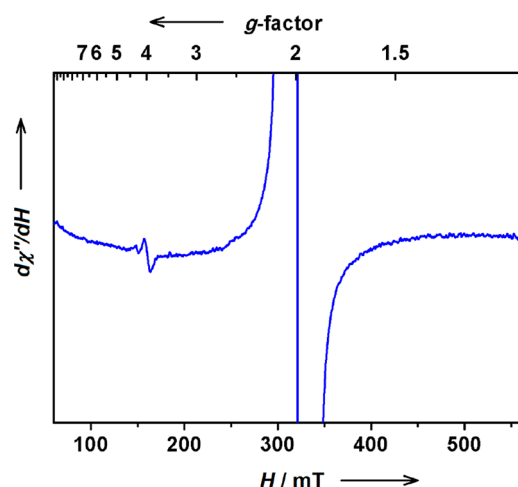


Figure 9. Frozen solution ($\text{CH}_2\text{Cl}_2/\text{MeCN}$) X-band EPR spectrum of **3** measured at $T = 17$ K. Microwave power of 1.0 mW and modulation of 1.0 mT were used to emphasize weak $|\Delta M_S| = 2$ transition at $g \approx 4$.

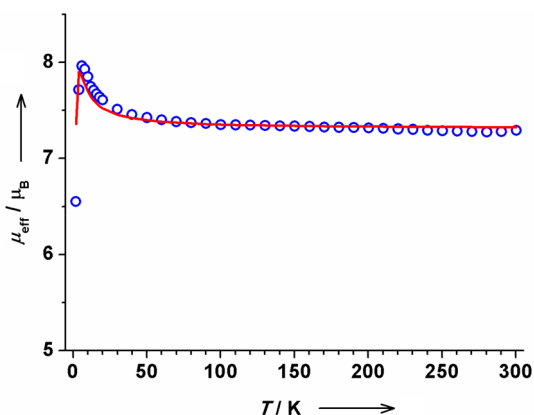


Figure 10. Temperature-dependent effective magnetic moment of **1** measured at external magnetic field $H = 1.0$ T. Red curve is the best fit obtained with $S_1 = S_2 = 2$, $g_1 = g_2 = 2.109$, and $J_{12} = +0.22 \text{ cm}^{-1}$.

μ_B is only consistent with two essentially uncoupled “monomeric units”, each containing a $hs\text{-Fe(III)}$ ion ($S = 5/2$) coupled strongly antiferromagnetically (exchange coupling constant $|J| > 150 \text{ cm}^{-1}$; $\hat{H} = -2J\hat{S}_1\hat{S}_2$) with a ligand π -radical (S

$= 1/2$). Such electronic configuration would give two noninteracting effective spins $S_1 = S_2 = 2$, with a spin-only estimate of $6.93 \mu_B$. Any other combination of the oxidation and spin states of iron ions would give a much larger or much smaller than determined magnetic moment. The increasing moment at low temperatures points to additional weak ferromagnetic interactions in the solid, which could be either intermolecular or intramolecular between the two $hs\text{-Fe(III)} + \text{R}^\bullet$ monomeric units, with the latter being more likely (vide infra). Magnetic data were fitted according to the model of two weakly coupled $S_1 = S_2 = 2$ system (Figures 10 and S5), which yields weak ferromagnetic interaction between the monomers with $J = +0.22 \text{ cm}^{-1}$. Interestingly, the rapid drop of magnetic moment at $T < 6$ K was reproduced with our simple model, which points to a saturation effect. Variable-field measurements at $T = 2$ K revealed (Figure S6, Supporting Information) the reduced magnetization tending to a plateau corresponding to an $S = 4$ ground state, which supports our model. The model has been further confirmed by the results of X-ray crystallography and Mössbauer spectroscopy (vide supra).

Magnetic susceptibility data collected on **2** reveal a room temperature magnetic moment of $2.66 \mu_B$, which increases gradually upon decreasing the temperature and reaches the maximum of $2.94 \mu_B$ at 8 K, followed by a slight drop at lower temperatures (Figure 11). The room temperature value is in

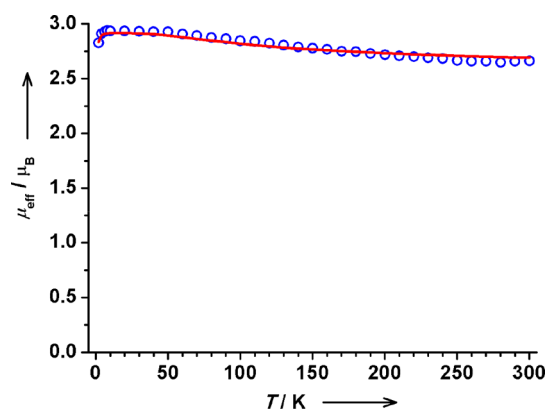


Figure 11. Temperature-dependent effective magnetic moment of **2** measured at external magnetic field $H = 1.0$ T. Red curve is the best fit obtained with $S_1 = S_2 = 1/2$, $g_1 = g_2 = 1.995$ (fixed, from EPR), $J = +47 \text{ cm}^{-1}$, paramagnetic impurity = 8.0% (modeled as $S = 3/2$ species with a molecular weight equal to 2; note that a genuine percentage should be much lower due to expected lower weight of this inorganic impurity).

good agreement with essentially noninteracting $S_1 = S_2 = 1/2$ spin system (spin-only estimate is $2.45 \mu_B$) slightly contaminated by a paramagnetic impurity. Note that it would not be possible to distinguish between the two electronic configurations: (A) essentially uncoupled monomeric units of $ls\text{-Co(III)}$ ($S = 0$) with a ligand π -radical ($S = 1/2$) and (B) essentially uncoupled monomeric units of $ls\text{-Co(II)}$ ($S = 1/2$) with a closed-shell ligand, relying only on magnetic data. However, the results from X-ray crystallography and EPR spectroscopy unambiguously confirm the electronic configuration A for this complex. The increasing moment at low temperatures points to significant ferromagnetic interactions in the solid state. Magnetic data were fitted according to an interacting $S_1 = S_2 = 1/2$ spin model (Figures 11 and S7),

which yields moderate ferromagnetic interactions between the monomeric units with $J = +47 \text{ cm}^{-1}$. Magnetic data acquired on **3** (Figure S8) are very similar to those of **2**. The fitting according to $S_1 = S_2 = 1/2$ spin system yields a similar ferromagnetic interaction between the monomeric $ls\text{-Co(III)-R}^\bullet$ units in **3** with $J = +47 \text{ cm}^{-1}$.

Theoretical Calculations. Electronic structures of **1–3** were examined by DFT calculations. The central point of these studies was the assignment of bands in electronic absorption spectra. The calculations were performed on slightly simplified models with all *tert*-Bu groups truncated to Me groups. The geometries of the complexes were fully optimized to broken-symmetry states BS(10,2) and BS(1,1) for iron and cobalt species, respectively, using the B3LYP functional.^{28,29} The optimized structures are in good agreement with the corresponding experimental structures obtained from X-ray crystallography (vide supra).

Spin density distributions reveal two couples of *hs*-Fe(III) ions with ligand π -radicals for **1** (Figure 12) and two

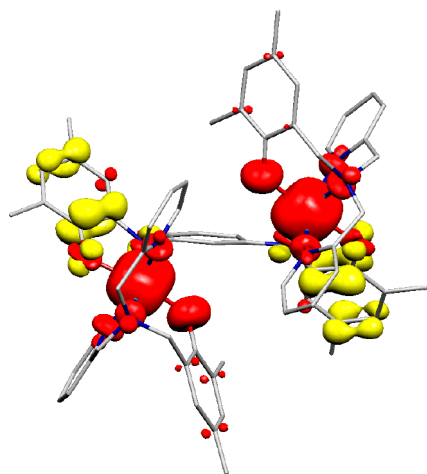


Figure 12. Spin density map for **1** showing a broken-symmetry state BS(10,2).

diamagnetic *ls*-Co(III) ions with two ligand π -radicals for **2** (Figure 13). The distribution of unpaired electron density in **3** (Figure S9) is very similar to that in **2**. Interestingly, the straightforward calculations with B3LYP reproduced qualitatively spin–spin coupling patterns deduced from magnetic

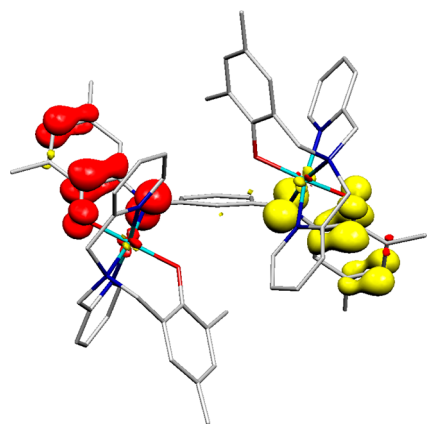


Figure 13. Spin density map for **2** showing a broken-symmetry state BS(1,1).

measurements (vide supra). Thus, the coupling between *hs*-Fe(III) ions and ligand radicals in **1** was predicted^{44–46} to be antiferromagnetic with $J_{\text{eff}} = -87 \text{ cm}^{-1}$ (here, J_{eff} is an effective exchange coupling constant between an effective iron-based $S = 5$ and an effective ligand-based $S = 1$ subsystem). The ferromagnetic coupling between two ligand radicals in cobalt complexes was reproduced, as well; the coupling constants were calculated at +110 and +100 cm^{-1} for **2** and **3**, respectively. We ascribe the ferromagnetic coupling in cobalt species to the efficient spin-polarization effect through a *meta*-phenylene bridge.

The electronic absorption spectra of **1–3** were calculated in the framework of the TD-DFT method using the same B3LYP. Due to the relatively large size of the systems, only the first 40 excited states were calculated for each complex. As expected, the large size and low symmetry of the molecules resulted in many closely spaced calculated excitations, which render the assignment of absorption bands in experimental spectra difficult. However, some qualitative interpretations could be done. All species absorb strongly in the near-infrared (NIR) region by showing bands centered in the 750–850 nm region (Figures 14, 15, and S10), which are in good agreement with

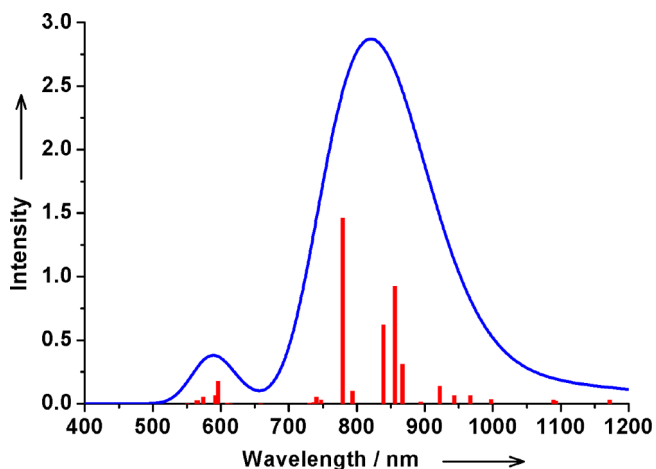


Figure 14. Electronic absorption spectrum of **1** (BS(10,2) state) obtained from spin-unrestricted B3LYP-TD-DFT calculations. The first 40 excited states were calculated; the full width at half-maximum was set to 2000 cm^{-1} for each transition.

the experimental data (vide supra). The analyses of the strongest excitations reveal that $\pi\text{-}\pi^*$ transitions within ligand π -radicals and LLCT transitions contribute strongly to those NIR bands (Figures S11–S13).

Electrochemistry. Cyclic voltammograms of complexes **1–3** have been recorded at a glassy carbon working electrode under an atmosphere of purified dinitrogen in acetonitrile solution (0.1 M TBAP) at 25 °C in the potential range from -2.0 V to $+2.0 \text{ V}$ vs Ag/AgCl. All potentials reported in this Article are referenced to Ag/AgCl. The collected data are summarized in Table 4. The CV of complex **1** exhibits two reversible redox processes (Figure 16a) at $(E_{1/2})_I = 0.06 \text{ V}$ with $\Delta E_p = 59 \text{ mV}$ (process I) and at $(E_{1/2})_{II} = -0.11 \text{ V}$ with $\Delta E_p = 59 \text{ mV}$ (process II). The normal pulse (Figure 16b) and differential pulse voltammograms (Figure 16c) of this complex indicate that both processes involve an identical number of electron(s). Figure 16c also indicates that both processes are cathodic, involving negative current heights which have been verified subsequently by steady-state voltammetry. Thus

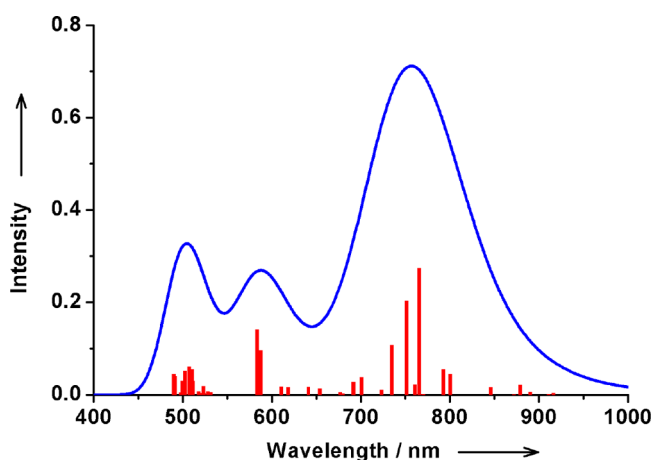


Figure 15. Electronic absorption spectrum of **2** (BS(1,1) state) obtained from spin-unrestricted B3LYP-TD-DFT calculations. The first 40 excited states were calculated; the full width at half-maximum was set to 2000 cm^{-1} for each transition.

process I with $E_{1/2}$ at a positive potential is confirmed to be a reduction process like process II, which appears at a negative potential. Considering **1** to be a diferric complex bridged by a noninnocent iminosemiquinone biradical moiety, any of the observed two reductions could either be a metal-based $[\text{Fe(III)}/\text{Fe(II)}]$ or a ligand-centered $[\text{L}^{\text{ISQ}\cdot\cdot}/\text{L}^{\text{AP}}]$ process. We did extensive combined coulometry/EPR experiments to understand the nature of these electron transfers. Thus, the electron stoichiometry of process I was further examined by controlled potential coulometry (CPC) experiments with a platinum gauze working electrode. The reduction at a working potential (E_{W}) of 0 V vs Ag/AgCl was found to be incomplete ($n = 0.69 \pm 0.08$) due to the overlapping nature of processes I and II in the voltammogram (Figure 16a). The catholyte solution was found to be EPR inactive. However, when the E_{W} was set at -0.3 V , well beyond the $(E_{1/2})_{\text{IV}}$, the CPC experiments proceed smoothly up to the completion and involve the consumption of $2.1 \pm 0.09\text{ F mol}^{-1}$. The steady-state voltammetric experiments done with the solutions (using an ultra-micro-platinum electrode, $10\text{ }\mu\text{M}$ in diameter) before and after the coulometric experiments indicate that the two-electron reduced product is quite stable. The catholyte solution is also EPR inactive, which is not unexpected considering **1** to be a multielectronic system, as revealed from its EPR, magnetic, and Mössbauer spectroscopic studies (vide supra).

The CVs and normal pulse voltammetries (NPVs) of the dicobalt(III) complexes **2** and **3** are nearly identical. A set of voltammograms for complex **2** is shown in Figure 17 as a representative type and those of **3** in Figure S14 (Supporting Information), each displaying four electrochemical responses, two in the cathodic (processes I and II) and two in the anodic regions (processes III and IV). In the scan rate range of 50–

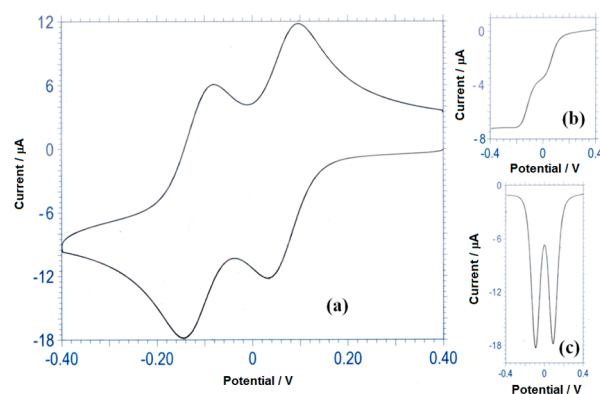


Figure 16. (a) Cyclic, (b) normal pulse, and (c) differential pulse voltammograms of compound **1** in acetonitrile.

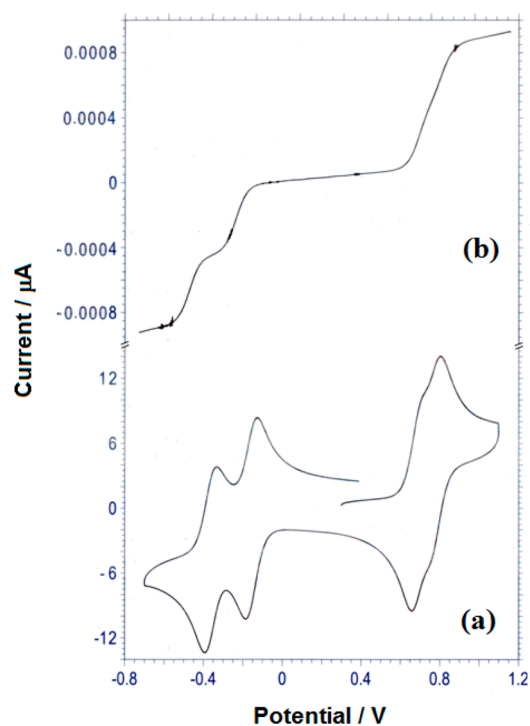


Figure 17. (a) Cyclic and (b) normal pulse voltammograms of compound **2** in acetonitrile solvent. Potentials vs Ag/AgCl, 0.1 M TBAP at a glassy carbon working electrode, scan rate = 200 mV s^{-1} .

500 mV s^{-1} , all of these electron transfers conform to the criteria of Nernstian reversibility. Interestingly, unlike that of compounds **2** and **3**, the anodic region in the voltammogram of **1** is featureless, displaying a broad irreversible process (Figure S15). The reduction processes in the CV of **2** appear at $(E_{1/2})_{\text{I}} = -0.16\text{ V}$ with $\Delta E_{\text{p}} = 54\text{ mV}$ (process I) and at $(E_{1/2})_{\text{II}} = -0.36\text{ V}$ with $\Delta E_{\text{p}} = 58\text{ mV}$ (process II). Corresponding

Table 4. Summary of Electrochemical Data^a for Complexes 1, 2, and 3

complex	process I		process II		process III		process IV	
	$(E_{1/2})_{\text{I}}/\text{V}^b$	$\Delta E_{\text{p}}/\text{mV}^c$	$(E_{1/2})_{\text{II}}/\text{V}^b$	$\Delta E_{\text{p}}/\text{mV}^c$	$(E_{1/2})_{\text{III}}/\text{V}^b$	$\Delta E_{\text{p}}/\text{mV}^c$	$(E_{1/2})_{\text{IV}}/\text{V}^b$	$\Delta E_{\text{p}}/\text{mV}^c$
1	0.06	59	-0.11	59				
2	-0.16	54	-0.36	58	0.68	50	0.78	42
3	-0.10	57	-0.22	63	0.75	57	0.85	52

^aAll potentials vs Ag/AgCl. ^b $E_{1/2} = 0.5(E_{\text{pc}} + E_{\text{pa}})$, calculated from CV data. ^c $\Delta E_{\text{p}} = E_{\text{pa}} - E_{\text{pc}}$ at a scan rate of 200 mV s^{-1} .

processes with **3** appear at -0.10 and -0.22 V, respectively. Due to their overlapping nature, the ΔE_p values for the redox processes in **2** are difficult to evaluate accurately. The oxidation processes also overlap in both **2** and **3**. In complex **2**, the oxidations appear at $(E_{1/2})_{\text{III}} = +0.68$ V and $(E_{1/2})_{\text{IV}} = +0.78$ V. As revealed from Table 4, the substitutions (Me vs Cl) in the facially coordinating ligand $[L^R]^{1-}$ make the reductions easier and oxidations difficult in **3** compared to **2**. Also, all of these four processes involve an identical number of electron(s) as established by NPV, as shown in Figure 17. Their differential pulse voltammograms shown in Figures 18 and S16 indicate

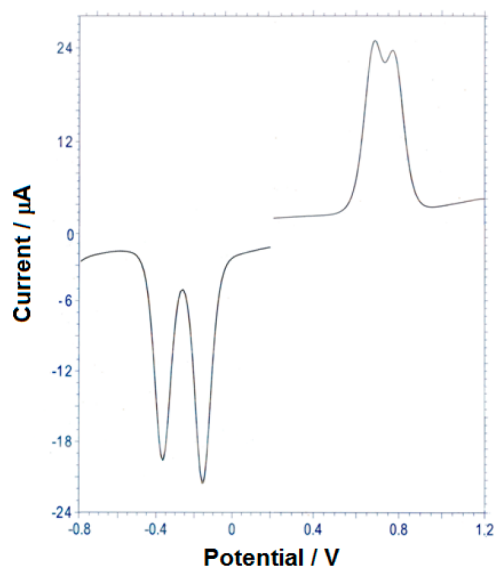


Figure 18. Differential pulse voltammogram of compound **2** in acetonitrile at 298 K; peak to peak amplitude is 25 mV.

that, while processes I and II are due to reduction, the latter two processes III and IV are due to oxidations, which is also confirmed later by steady-state voltammetry. In order to diagnose the nature of these four-electron transfer processes conclusively, we decided to carry out combined coulometry/EPR experiments as we did for **1**. We preferred to use compound **2** as a representative of the two for these experiments considering its relatively clean CV with less overlapping features. In a stirred acetonitrile solution, as evident from constant potential coulometric experiments, the reduction of **2** occurred smoothly with $n = 1 \pm 0.05$ when the working potential (E_W) was set at -0.25 V. The catholyte solution is EPR active and displayed a well-resolved eight-line EPR spectrum at 77 K (Figure 19) centered at $\langle g \rangle = 1.991$ due to ^{59}Co ($I = 7/2$) hyperfine coupling⁴⁷ with $a_{\text{Co}} = 10.7$ G. The data confirm this reduction process to be a ligand-based one. Unfortunately, the results of the coulometry experiments done at a E_W set at -0.6 V were vitiated by constant coulomb counts due to unidentified electrode reaction(s). However, a one-electron reduction involving a ligand-based orbital ($L^{\text{ISQ}\cdot} \rightarrow L^{\text{AP}}$) was proposed by combining the results of normal and differential pulse voltammetry (Figures 17 and 18) as well as those of the coulometric experiments done in the cathodic range.

Because the oxidation processes (III and IV) are overlapping in both complexes (Figures 17 and S14), the combined electron stoichiometry for these processes was determined by coulometric experiments done at a potential well beyond the

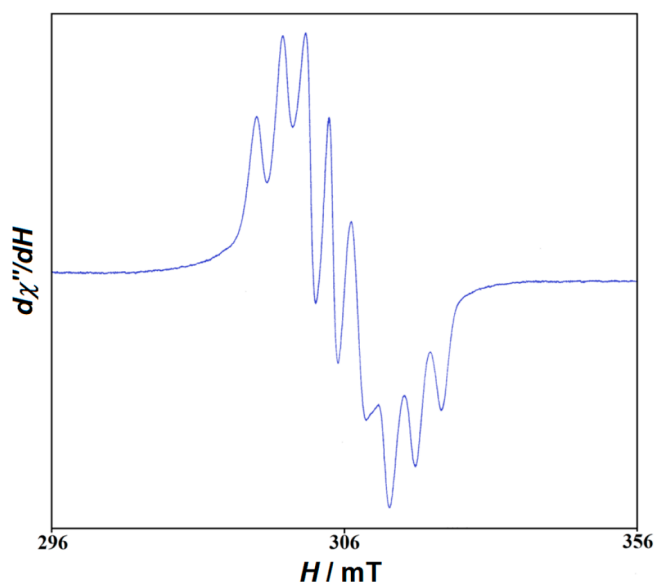


Figure 19. EPR spectrum at 77 K of the catholyte solution generated during the one-electron reduction of **2** by controlled-potential electrolysis; E_W set at -0.25 V vs Ag/AgCl reference (frequency = 9.11 GHz; modulation = 0.7 mT; power = 1.0 mW).

oxidation process IV (E_W set at 1.0 V vs Ag/AgCl). The results ($n = 2.03 \pm 0.05$) are in conformity with the two-electron stoichiometry for these processes, thus endorsing the individual processes (III and IV) to be monoelectronic. Steady-state voltammetric experiments done with the solution before and after the coulometric oxidation indicate that the oxidized product is quite stable. The anolyte solution after two-electron oxidation appears to also be EPR inactive. This is as expected considering that both oxidation processes are ligand based ($L^{\text{ISQ}\cdot} \rightarrow L^{\text{IBQ}}$).

The electrochemical results with the cobalt(III) compounds **2** and **3** thus indicate the involvement of four one-electron transfer processes, all involving the redox noninnocent biradical ligand as summarized by eqs 1–4. In the case of the iron(III) complex **1**, the oxidation processes (III and IV) are missing due to unknown reason(s).



CONCLUSIONS

Syntheses of rare biradical-bridged complexes $[(L^R)\text{M}^{\text{III}}(\bullet L^B \bullet)\text{-M}^{\text{III}}(L^R)][\text{ClO}_4]_2$, $M = \text{Fe}$ (**1**) and Co (**2**, **3**), have been reported. The identities of these compounds are established by single-crystal X-ray diffraction analysis, which supports the iminobenzosemiquinone ($L^{\text{ISQ}}\text{-}L^{\text{ISQ}}$) oxidation level of the biradical bridge. The electronic structures of **1**–**3** were probed by magnetic measurements and Mössbauer and EPR spectroscopy. These studies confirmed the biradical (iminobenzosemiquinone) nature ($\bullet L^B \bullet$) of the bridging L^B ligand and +3 oxidation states for metal ions throughout the series **1**–**3**.

Interestingly, both Fe(III) ions in **1** adopt a high-spin state ($S = 5/2$) and become each strongly antiferromagnetically coupled with a corresponding ligand π -radical. However, Co(III) ions in **2** and **3** are low spin ($S = 0$), which allows for a moderate ferromagnetic coupling ($J = +47 \text{ cm}^{-1}$) within two $S = 1/2$ spins of the biradical bridge. Similar ferromagnetic coupling ($J = +85(S) \text{ cm}^{-1}$) has been reported recently for a dinuclear Ru(II) complex of the same bridging ligand.⁴⁸ Electrochemical measurements demonstrate smooth multiple electron transfers within these complexes, all involving the redox noninnocent iminobenzosemiquinone bridge. The high flexibility and diversity of electronic structures in the reported metal complexes (high vs low spin, antiferromagnetic vs ferromagnetic coupling) call for further exploration of these types of binuclear metal complexes in the context of magnetic and bistable materials.

■ ASSOCIATED CONTENT

Supporting Information

The Supporting Information is available free of charge on the ACS Publications website at DOI: 10.1021/acs.inorgchem.7b02340.

Partially labeled perspective view of the crystal structure of **3** (Figure S1), views of the extended solid-state structures of **2** and **3** (Figure S2), EPR spectra of **3** in solution at room temperature and in the frozen solution (Figure S3) and that of **2** at 17 K in the half-field region (Figure S4), magnetic data acquired on complexes **1**–**3** (Figures S5–S8), spin density distribution (Figure S9), theoretical vis–NIR spectrum (Figure S10), and assignment of electronic spectral bands (Figures S11–S13) through DFT calculation, and cyclic, normal pulse, and differential pulse voltammograms of **1**–**3** (Figures S14–S16) (PDF)

Accession Codes

CCDC 1564857–1564859 contain the supplementary crystallographic data for this paper. These data can be obtained free of charge via www.ccdc.cam.ac.uk/data_request/cif, or by emailing data_request@ccdc.cam.ac.uk, or by contacting The Cambridge Crystallographic Data Centre, 12 Union Road, Cambridge CB2 1EZ, UK; fax: +44 1223 336033.

■ AUTHOR INFORMATION

Corresponding Authors

*E-mail: icmc@iacs.res.in (M.C.).

*E-mail: marat.khusniyarov@fau.de (M.M.K.).

ORCID

Marat M. Khusniyarov: 0000-0002-2034-421X

Muktimoy Chaudhury: 0000-0002-6069-1072

Notes

The authors declare no competing financial interest.

■ ACKNOWLEDGMENTS

This work was supported by the Council of Scientific and Industrial Research (CSIR), New Delhi (Grant No. 01/2557/12-EMR-II). D.M. and M.C.M. also thank the CSIR for the award of Research Fellowships. The single-crystal X-ray diffraction data were collected on an instrument supported by DST, New Delhi, as a National Facility at IACS under the IRHPA program. G.A. is grateful to the Alexander von Humboldt (AvH) Foundation for a Georg Forster Research

Fellowship. M.M.K. thanks the Fonds der Chemischen Industrie (FCI, Liebig Fellowship), Deutsche Forschungsgemeinschaft (DFG Research Grant KH 279/3), and Emerging Talents Initiative (ETI) program of the FAU Erlangen-Nürnberg for financial support. Prof. Karsten Meyer (FAU Erlangen-Nürnberg) is acknowledged for providing access to spectroscopic facilities. Dr. Jörg Sutter (FAU Erlangen-Nürnberg) is acknowledged for Mössbauer spectral measurements.

■ REFERENCES

- (1) (a) Pierpont, C. G. Studies on charge distribution and valence tautomerism in transition metal complexes of catecholate and semiquinonate ligands. *Coord. Chem. Rev.* **2001**, *216–217*, 99–125. (b) Chirik, P. J. Preface: Forum on redox-active ligands. *Inorg. Chem.* **2011**, *50*, 9737–9740. (c) Kaim, W. The shrinking world of innocent ligands: conventional and non-conventional redox-active ligands. *Eur. J. Inorg. Chem.* **2012**, *2012*, 343–348. (d) Luca, O. R.; Crabtree, R. H. Redox-active ligands in catalysis. *Chem. Soc. Rev.* **2013**, *42*, 1440–1459. (e) Praneeth, V. K. K.; Ringenberg, M. R.; Ward, T. R. Redox-active ligands in catalysis. *Angew. Chem., Int. Ed.* **2012**, *51*, 10228–10234. (f) Chirik, P. J.; Wieghardt, K. Radical ligands confer nobility on base-metal catalysts. *Science* **2010**, *327*, 794–795. (g) Koivisto, B. D.; Hicks, R. G. The magnetochemistry of verdazyl radical-based materials. *Coord. Chem. Rev.* **2005**, *249*, 2612–2630. (h) Vostrikova, K. E. High-spin molecules based on metal complexes of organic free radicals. *Coord. Chem. Rev.* **2008**, *252*, 1409–1419. (i) Sproules, S.; Wieghardt, K. Dithiolene radicals: Sulfur K-edge X-ray absorption spectroscopy and Harry's intuition. *Coord. Chem. Rev.* **2011**, *255*, 837–860.
- (2) (a) Bryliakov, K. P.; Talsi, E. P. Active sites and mechanisms of bioinspired oxidation with H_2O_2 , catalyzed by non-heme Fe and related Mn complexes. *Coord. Chem. Rev.* **2014**, *276*, 73–96. (b) Costas, M.; Mehn, M. P.; Jensen, M. P.; Que, L. Dioxxygen activation at mononuclear nonheme iron active sites: enzymes, models, and intermediates. *Chem. Rev.* **2004**, *104*, 939–986. (c) Jazdzewski, B. A.; Tolman, W. B. Understanding the copper–phenoxyl radical array in galactose oxidase: contributions from synthetic modeling studies. *Coord. Chem. Rev.* **2000**, *200–202*, 633–685. (d) Stone, K. L.; Borovik, A. S. Lessons from nature: unraveling biological C–H bond activation. *Curr. Opin. Chem. Biol.* **2009**, *13*, 114–118. (e) Groves, J. T. Enzymatic C–H bond activation: Using push to get pull. *Nat. Chem.* **2014**, *6*, 89–91.
- (3) Jørgensen, C. K. Differences between the four halide ligands, and discussion remarks on trigonal-bipyramidal complexes, on oxidation states, and on diagonal elements of one-electron energy. *Coord. Chem. Rev.* **1966**, *1*, 164–178.
- (4) Kaim, W.; Schwederski, B. Non-innocent ligands in bioinorganic chemistry - An overview. *Coord. Chem. Rev.* **2010**, *254*, 1580–1588.
- (5) (a) Dei, A.; Gatteschi, D.; Sangregorio, C.; Sorace, L. Quinonoid metal complexes: toward molecular switches. *Acc. Chem. Res.* **2004**, *37*, 827–835. (b) Vázquez-Mera, N. A.; Novio, F.; Roscini, C.; Bellacanzone, Ch.; Guardingo, M.; Hernando, J.; Ruiz-Molina, D. Switchable colloids, thin-films and interphases based on metal complexes with non-innocent ligands: the case of valence tautomerism and their applications. *J. Mater. Chem. C* **2016**, *4*, 5879–5889.
- (6) Poddel'sky, A. I.; Cherkasov, V. K.; Abakumov, G. A. Transition metal complexes with bulky 4,6-di-*tert*-butyl-*N*-aryl(alkyl)-*o*-iminobenzquinonato ligands: Structure, EPR and magnetism. *Coord. Chem. Rev.* **2009**, *253*, 291–324.
- (7) Nakamura, N.; Moenne-Loccoz, P.; Tanizawa, K.; Mure, M.; Suzuki, S.; Klinman, J. P.; Sanders-Loehr, J. Topaquinone-dependent amine oxidases: identification of reaction intermediates by Raman spectroscopy. *Biochemistry* **1997**, *36*, 11479–11486.
- (8) Kishishita, S.; Okajima, T.; Kim, M.; Yamaguchi, H.; Hirota, S.; Suzuki, S.; Kuroda, S.; Tanizawa, K.; Mure, M. Role of copper ion in bacterial copper amine oxidase: spectroscopic and crystallographic studies of metal-substituted enzymes. *J. Am. Chem. Soc.* **2003**, *125*, 1041–1055.

- (9) (a) Kano, K.; Nakagawa, M.; Takagi, K.; Ikeda, T. Mechanistic study of amine oxidation catalysed by quinonoid cofactors. *J. Chem. Soc., Perkin Trans. 2* **1997**, 2, 1111–1120. (b) Carter, S. M.; Sia, A.; Shaw, M. J.; Heyduk, A. F. Isolation and characterization of a neutral imino-semiquinone radical. *J. Am. Chem. Soc.* **2008**, *130*, 5838–5839.
- (10) (a) Tezgerevska, T.; Alley, K. G.; Boskovic, C. Valence tautomerism in metal complexes: stimulated and reversible intramolecular electron transfer between metal centers and organic ligands. *Coord. Chem. Rev.* **2014**, *268*, 23–40. (b) Faust, T. B.; D'Alessandro, D. M. Radicals in metal–organic frameworks. *RSC Adv.* **2014**, *4*, 17498–17512. (c) Ratera, I.; Veciana, J. Playing with organic radicals as building blocks for functional molecular materials. *Chem. Soc. Rev.* **2012**, *41*, 303–349. (d) Demir, S.; Jeon, I.-R.; Long, J. R.; Harris, T. D. Radical ligand-containing single-molecule magnets. *Coord. Chem. Rev.* **2015**, *289–290*, 149–176.
- (11) (a) Miller, J. S.; Min, K. S. Oxidation leading to reduction: redox-induced electron transfer (RIET). *Angew. Chem., Int. Ed.* **2009**, *48*, 262. (b) Min, K. S.; DiPasquale, A. G.; Golen, J. A.; Rheingold, A. L.; Miller, J. S. Synthesis, structure, and magnetic properties of valence ambiguous dinuclear antiferromagnetically coupled cobalt and ferromagnetically coupled iron complexes containing the chloranilate(2–) and the significantly stronger coupling chloranilate(•3–) radical trianion. *J. Am. Chem. Soc.* **2007**, *129*, 2360–2368. (c) Darago, L. E.; Aubrey, M. L.; Yu, C. J.; Gonzalez, M. I.; Long, J. R. Electronic conductivity, ferrimagnetic ordering, and reductive insertion mediated by organic mixed-valence in a ferric semiquinoid metal–organic framework. *J. Am. Chem. Soc.* **2015**, *137*, 15703–15711. (d) Kitagawa, S.; Kawata, S. Coordination compounds of 1,4-dihydroxybenzoquinone and its homologues. Structures and properties. *Coord. Chem. Rev.* **2002**, *224*, 11–34. (e) van der Meer, M.; Rechkemmer, Y.; Breitgoff, F. D.; Marx, R.; Neugebauer, P.; Frank, U.; van Slageren, J.; Sarkar, B. Multiple Bistability in Quinonoid-Bridged Diiron(II) Complexes: Influence of Bridge Symmetry on Bistable Properties. *Inorg. Chem.* **2016**, *55*, 11944–11953. (f) van der Meer, M.; Rechkemmer, Y.; Frank, U.; Breitgoff, F. D.; Hohloch, S.; Su, C.-Y.; Neugebauer, P.; Marx, R.; Dörfel, M.; van Slageren, J.; Sarkar, B. A Dicobalt Complex with an Unsymmetrical Quinonoid Bridge Isolated in Three Units of Charge: A Combined Structural, (Spectro)electrochemical, Magnetic and Spectroscopic Study. *Chem. - Eur. J.* **2016**, *22*, 13884–13893.
- (12) Jeon, I.-R.; Park, J. G.; Xiao, D. J.; Harris, T. D. An Azophenine radical-bridged Fe₂ single-molecule magnet with record magnetic exchange coupling. *J. Am. Chem. Soc.* **2013**, *135*, 16845–16848.
- (13) Alley, K. G.; Poneti, G.; Robinson, P. S. D.; Nafady, A.; Moubaraki, B.; Aitken, J. B.; Drew, S. C.; Ritchie, C.; Abrahams, B. F.; Hocking, R. K.; Murray, K. S.; Bond, A. M.; Harris, H. H.; Sorace, L.; Boskovic, C. Redox activity and two-step valence tautomerism in a family of dinuclear cobalt complexes with a spiroconjugated bis(dioxolene) ligand. *J. Am. Chem. Soc.* **2013**, *135*, 8304–8323.
- (14) DeGayner, J. A.; Jeon, I.-R.; Harris, T. D. A series of tetraazalene radical-bridged M₂ (M = Cr^{III}, Mn^{II}, Fe^{II}, Co^{II}) complexes with strong magnetic exchange coupling. *Chem. Sci.* **2015**, *6*, 6639–6648.
- (15) Fatila, E. M.; Clerac, R.; Rouzies, M.; Soldatov, D. V.; Jennings, M.; Preuss, K. E. High-spin ribbons and antiferromagnetic ordering of a Mn^{II}-biradical-Mn^{II} complex. *J. Am. Chem. Soc.* **2013**, *135*, 13298–13301.
- (16) Poneti, G.; Mannini, M.; Cortigiani, B.; Poggini, L.; Sorace, L.; Otero, E.; Sainctavit, P.; Sessoli, R.; Dei, A. Magnetic and spectroscopic investigation of thermally and optically driven valence tautomerism in thioether-bridged dinuclear cobalt–dioxolene complexes. *Inorg. Chem.* **2013**, *52*, 11798–11805.
- (17) Sarkar, B.; Schweinfurth, D.; Deibel, N.; Weisser, F. Functional metal complexes based on bridging “imino”-quinonoid ligands. *Coord. Chem. Rev.* **2015**, *293–294*, 250–262.
- (18) Shultz, D. A.; Bodnar, S. H.; Lee, H.; Kampf, J. W.; Incarvito, C. D.; Rheingold, A. L. Singlet–triplet gap in triplet ground-state biradicals is modulated by substituent effects. *J. Am. Chem. Soc.* **2002**, *124*, 10054–10061.
- (19) (a) Caneschi, A.; Dei, A.; Lee, H.; Shultz, D. A.; Sorace, L. Ferromagnetically coupled bis(semiquinone) ligand enforces high-spin ground states in bis-metal complexes. *Inorg. Chem.* **2001**, *40*, 408.
- (20) Dei, A.; Gatteschi, D.; Sangregorio, C.; Sorace, L.; Vaz, M. G. F. Bonding coordination requirements induce antiferromagnetic coupling between m-phenylene bridged o-iminosemiquinonato diradicals. *Inorg. Chem.* **2003**, *42*, 1701–1706.
- (21) Perrin, D. D.; Armarego, W. L. F.; Perrin, D. R. *Purification of Laboratory Chemicals*, 2nd ed.; Pergamon: Oxford, U.K., 1980.
- (22) Tshuva, E. Y.; Goldberg, I.; Kol, M.; Goldschmidt, Z. Zirconium complexes of amine–bis(phenolate) ligands as catalysts for 1-hexene polymerization: peripheral structural parameters strongly affect reactivity. *Organometallics* **2001**, *20*, 3017–3028. (b) Lubben, M.; Feringa, B. L. A new method for the synthesis of nonsymmetric dinucleating ligands by aminomethylation of phenols and salicylaldehydes. *J. Org. Chem.* **1994**, *59*, 2227–2233.
- (23) Robinson, W. R. Perchlorate salts of metal ion complexes: Potential explosives. *J. Chem. Educ.* **1985**, *62*, 1001.
- (24) Gagne, R. R.; Koval, C. A.; Lisensky, G. C. Ferrocene as an internal standard for electrochemical measurements. *Inorg. Chem.* **1980**, *19*, 2854–2855.
- (25) Bill, E. *MFIT*, version 1.1; MPI for Bioinorganic Chemistry; Muelheim/Ruhr, Germany, 2008.
- (26) Bill, E. *JulX*, version 1.5; MPI for Bioinorganic Chemistry; Muelheim/Ruhr, Germany, 2008.
- (27) Neese, F. *ORCA 4.0.0-Ab Initio*, DFT and semiempirical electronic structure package; Max Planck Institute for Chemical Energy Conversion, Muelheim/Ruhr, Germany.
- (28) Lee, C. T.; Yang, W. T.; Parr, R. G. Development of the Colle-Salvetti Correlation-Energy Formula into a Functional of the Electron-Density. *Phys. Rev. B: Condens. Matter Mater. Phys.* **1988**, *37* (2), 785–789.
- (29) Becke, A. D. Density-Functional Thermochemistry. 3. The Role of Exact Exchange. *J. Chem. Phys.* **1993**, *98* (7), 5648–5652.
- (30) Weigend, F.; Ahlrichs, R. Balanced basis sets of split valence, triple zeta valence and quadruple zeta valence quality for H to Rn: Design and assessment of accuracy. *Phys. Chem. Chem. Phys.* **2005**, *7* (18), 3297–3305.
- (31) Weigend, F. Accurate Coulomb-fitting basis sets for H to Rn. *Phys. Chem. Chem. Phys.* **2006**, *8* (9), 1057–1065.
- (32) Portmann, S. *Molekel*, version 4.3.win32; CSCS/UNI Geneva: Switzerland, 2002.
- (33) *SADABS*, version 2.03; Bruker AXS Inc.: Madison, WI, 2002.
- (34) Sheldrick, G. M. Phase annealing in *SHELX-90*: direct methods for larger structures. *Acta Crystallogr., Sect. A: Found. Crystallogr.* **1990**, *46*, 467.
- (35) Sheldrick, G. M. *SHELXL-2013*; University of Gottingen: Gottingen, Germany, 2013.
- (36) *SAINT*, version 6.02; Bruker AXS Inc.: Madison, WI, 2002.
- (37) *DIAMOND*, version 3.1; visual crystal structure information system; Crystal Impact: Bonn, Germany, 2004.
- (38) (a) Snodin, M. D.; Ould-Moussa, L.; Wallmann, U.; Lecomte, S.; Bachler, V.; Bill, E.; Hummel, H.; Weyhermuller, T.; Hildebrandt, P.; Wieghardt, K. The molecular and electronic structure of octahedral tris(phenolato)iron(III) complexes and their phenoxyl radical analogues: a mössbauer and resonance raman spectroscopic study. *Chem. - Eur. J.* **1999**, *5*, 2554–2565. (b) Marlin, D. S.; Mascharak, P. K. Coordination of carboxamido nitrogen to trivalent iron: insight into a new chapter of iron chemistry. *Chem. Soc. Rev.* **2000**, *29*, 69–74.
- (39) (a) Brown, S. N. Metrical oxidation states of 2-amidophenoxide and catecholate ligands: structural signatures of metal–ligand π bonding in potentially noninnocent ligands. *Inorg. Chem.* **2012**, *51*, 1251–1260. (b) Chaudhuri, P.; Verani, C. N.; Bill, E.; Bothe, E.; Weyhermuller, T.; Wieghardt, K. Electronic structure of bis(o-iminobenzosemiquinonato)metal complexes (Cu, Ni, Pd). The art of establishing physical oxidation states in transition-metal complexes containing radical ligands. *J. Am. Chem. Soc.* **2001**, *123*, 2213–2223. (c) Ye, S. F.; Sarkar, B.; Duboc, C.; Fiedler, J.; Kaim, W. The Redox Series [M(bpy)₂(Q)]ⁿ⁺, M = Ru or Os, Q = 3,5-Di-tert-butyl-N-

phenyl-1,2-benzoquinonemonoimine. Isolation and a Complete X and W Band EPR Study of the Semiquinone States ($n = 1$). *Inorg. Chem.* **2005**, *44*, 2843–2847.

(40) Verani, C. N.; Gallert, S.; Bill, E.; Weyhermüller, T.; Wieghardt, K.; Chaudhuri, P. [Tris(*o*-iminosemiquinone)cobalt(III)]—a radical complex with an $S_t = 3/2$ ground state. *Chem. Commun.* **1999**, 1747–1748.

(41) (a) Yan, S.; Que, L., Jr.; Taylor, L. F.; Anderson, O. P. A model for the chromophoric site of purple acid phosphatases. *J. Am. Chem. Soc.* **1988**, *110*, 5222–5224. (b) Alhashmialameer, D.; Collins, J.; Hattenhauer, K.; Kerton, F. M. Iron amino-bis(phenolate) complexes for the formation of organic carbonates from CO_2 and oxiranes. *Catal. Sci. Technol.* **2016**, *6*, 5364–5373.

(42) Gütlich, P., Bill, E., Trautwein, A. X. *Mössbauer Spectroscopy and Transition Metal Chemistry: Fundamentals and Applications*; Springer: Berlin, 2011.

(43) Weil, J. A.; Bolton, J. R.; Wertz, J. E. *Electron Paramagnetic Resonance, Elementary Theory and Practical Applications*; Wiley: New York, 1994.

(44) Ginsberg, A. P. Magnetic Exchange in Transition-Metal Complexes 0.12. Calculation of Cluster Exchange Coupling-Constants with the X-Alpha-Scattered Wave Method. *J. Am. Chem. Soc.* **1980**, *102* (1), 111–117.

(45) Noodleman, L. Valence Bond Description of Anti-Ferromagnetic Coupling in Transition-Metal Dimers. *J. Chem. Phys.* **1981**, *74* (10), 5737–5743.

(46) Noodleman, L.; Davidson, E. R. Ligand Spin Polarization and Antiferromagnetic Coupling in Transition-Metal Dimers. *Chem. Phys.* **1986**, *109* (1), 131–143.

(47) Cador, O.; Chabre, F.; Dei, A.; Sangregorio, C.; Van Slageren, J.; Vaz, M. G. F. Temperature-induced solid-state valence tautomeric interconversion in two cobalt–schiff base diquinone complexes. *Inorg. Chem.* **2003**, *42*, 6432–6440.

(48) de Biani, F. F.; Dei, A.; Sangregorio, C.; Sorace, L. Dinuclear ruthenium bipyridine complexes with a bis(iminodioxolene)-metaphenylene ligand: magnetic coupling and mixed valence character of the semiquinonato species. *Dalton Trans.* **2005**, 3868–3873.